RSC Advances

PAPER

View Article Online
View Journal | View Issue

Cite this: *RSC Adv.*, 2017, 7, 4444

Band-tunable photodetectors based on graphene/alloyed $Zn_xCd_{1-x}S$ film hybrids

Fan Huang,[a] Sheng Ouyang,[b] Feixiang Jia,[a] Caoyuan Cai,[a] Zhihao Xu,[a] Congjun Wu,[a]
Yang Ma[a] and Min Wang*[a]

Received 15th November 2016
Accepted 22nd December 2016

DOI: 10.1039/c6ra26823d

www.rsc.org/advances

Graphene/semiconductor film hybrid-based photodetectors have attracted extensive attention because of their ultra-high performance. However, only the photoconductive behavior of binary semiconductors with fixed bandgap was studied since achieving tunable optoelectronic properties is significant for the practical applications of semiconductors. Herein, alloyed $Zn_xCd_{1-x}S$ ($0 \leq x \leq 1$) films with complete compositional tunability were successfully prepared by an e-beam evaporation method *via* changing the molar ratio of ZnS to CdS in the target. UV-visible optical absorption measurements showed that the composition-dependent band-edge absorption is generated in the as-prepared alloyed $Zn_xCd_{1-x}S$ films, with the energy gaps continuously shifted from 2.41 eV ($x = 0$, CdS) to 3.67 eV ($x = 1$, ZnS). After graphene is transferred on the alloyed $Zn_xCd_{1-x}S$ films, band-tunable photodetectors are achieved based on graphene/alloyed $Zn_xCd_{1-x}S$ film hybrids with the cut-off wavelength in the spectral response gradually changing from 410 nm to 580 nm. Obviously, the method introduced in this study can be extended to fabricate other graphene/alloyed ternary film hybrid-based photodetectors with band tunability in the visible and infrared region.

1. Introduction

Photodetectors have attracted significant attention in recent years owing to their various applications in the fields such as communication, sensing, environmental protection, and imaging.[1–3] In terms of the dimensionality of photoactive material, these mainly include one-dimensional (1D) nanostructure-based and film-based photodetectors.[4–6] The film-based photodetectors possess a low performance due to the low carrier mobility of the film consisting of nanocrystals. Our previous studies and studies reported by other group have shown that the performance can be greatly enhanced by hybridizing semiconductor films with graphene, a two-dimensional single-layer of sp^2 bonded carbon atoms with ultra-high carrier mobility,[7–17] which can provide an ultra-fast transport channel for the photogenerated carriers of photoactive materials. Konstantatos *et al.* demonstrated a responsivity of 10^7 A W^{-1} in a photodetector based on graphene/PbS quantum dot hybrids.[9] This remarkable performance clearly shows the superiority of this approach. It is well known that for photoconductive devices, the detected light wavelength depends on the band gap of a photoactive semiconductor. Among these, only the photoconductive behavior of binary semiconductors with a fixed bandgap was studied. However, achieving tunable optoelectronic properties is significant for the practical applications of semiconductors. Therefore, it is desirable to achieve band-tunable graphene/semiconductor film hybrid-based photodetectors.

Alloying of binary semiconductors is an important approach to achieve tunable optoelectronic properties *via* composition modulation. Our previous study illustrates that $E_g(AB_xC_{1-x})$ (the energy gap of the alloyed AB_xC_{1-x}) can be continuously tuned from E_g(AB) (the energy gap of the binary compound AB) to E_g(AC) (the energy gap of the binary compound AC) as the composition x varies.[18] This approach has been widely utilized to obtain tunable optoelectronic properties including photoluminescence, lasing, and photocatalysis.[18–25] However, only few studies have reported nanowire-based band-tunable photodetectors based on the abovementioned bandgap engineering.[26–28] To the best of our knowledge, graphene/semiconductor film hybrid-based photodetectors with band tunability have never been reported.

In view of the tunable photoconductive properties of graphene/alloyed film hybrids, ternary $Zn_xCd_{1-x}S$ ($0 \leq x \leq 1$) is a good candidate. As a wide-gap II–VI semiconductor, ZnS and CdS have a bandgap of 3.67 eV and 2.41 eV, respectively, which implies that ZnS and CdS are potentially excellent photoactive materials for photodetectors. Several studies have investigated the photocatalytic activity and photoelectrochemical performance of the graphene/$Zn_xCd_{1-x}S$ hybrids.[29–31] In this study, we prepared alloyed wide bandgap $Zn_xCd_{1-x}S$ ($0 \leq x \leq 1$) films by e-beam evaporation method by changing the molar ratio of ZnS

---

[a] *School of Materials Science and Engineering, Hefei University of Technology, Tunxi Road 193, Hefei 230009, P. R. China. E-mail: minwang@hfut.edu.cn*

[b] *School of Physical Science and Technology, Lanzhou University, Lanzhou 730000, P. R. China*

to CdS in the target, and for the first time, examined the band-tunable photoconductive properties of graphene/alloyed $Zn_xCd_{1-x}S$ film hybrids.

2. Experimental

2.1. Preparation of the $Zn_xCd_{1-x}S$ film

ZnS (99.99% purity) and CdS (99.99% purity) powders with different molar ratios were mixed and ground in a grinding dish for 30 minutes. After this, the mixed powders were sintered at 950 °C for 1.5 hours with 10 sccm H_2 and 20 sccm Ar. With the sintered $Zn_xCd_{1-x}S$ powders as targets, the $Zn_xCd_{1-x}S$ film with a thickness of 60 nm was deposited on a 300 nm SiO_2/Si substrate by e-beam evaporation. The vacuum remained at 2×10^{-4} Pa during the entire deposition process. Before the graphene transfer, the $Zn_xCd_{1-x}S$ film on the Si/SiO_2 substrate was annealed for 30 min at 300 °C under low pressure with 10 sccm H_2 and 20 sccm Ar, enabling the film adhesion to the substrate as it was placed in water to pick up the graphene films.

2.2. Graphene growth and transfer

The details of graphene growth and transfer can be found in our previous studies,[32,33] except that the PMMA carrier for graphene transfer was removed by annealing for 2 hours at 400 °C under low pressure with 10 sccm H_2 and 20 sccm Ar. This method enables the crackless transfer of graphene.[17,34]

2.3. Transistor fabrication

After PMMA was removed, devices with a channel length of 20 μm and width of 500 μm were fabricated with a shadow mask. The doped Si substrate served as a global back gate. Cr/Au (10 nm/100 nm) was used as the electrical contact metal for the source and drain electrodes were deposited using a high-vacuum thermal evaporation system.

2.4. Characterization and measurement

The composition of $Zn_xCd_{1-x}S$ films was characterized *via* energy dispersive X-ray spectroscopy (EDX) using a Hitachi SU8020 scanning electron microscope and *via* X-ray photoelectron spectroscopy (XPS) (ESCALAB250Xi). XRD patterns of the samples were obtained using an X-ray diffractometer (X'Pert Pro MPD) with $\lambda = 1.54056$ Å. UV-vis absorption (UV-3600) was conducted on the samples after they were transferred on a quartz substrate. The microstructure of $Zn_xCd_{1-x}S$ was characterized by transmission electron microscopy (TEM) (Tecnai G2 F20). The electrical and photoconductive properties of the graphene/CdS film and graphene/$Zn_xCd_{1-x}S$ film hybrid devices were measured by a semiconductor parameter analyzer system (Keithley 2636B) at room temperature using light emitting diodes with the corresponding wavelength as the incident light.

3. Results and discussion

3.1. Surface information and composition

To investigate the surface information and determine the composition x of the as-deposited ternary $Zn_xCd_{1-x}S$ films, EDX mapping and XPS analysis was carried out. The uniform distribution of Zn, Cd, and S in the EDX mapping shows that the as-deposited film is $Zn_xCd_{1-x}S$ (Fig. 1a–c). Fig. 1d–f show the XPS survey spectra of the alloyed $Zn_xCd_{1-x}S$ films obtained by e-beam evaporation with the targets having various ZnS/CdS molar ratios of 2 : 8, 5 : 5, 7 : 3, 8 : 2, and 9 : 1. The XPS peaks of Zn $2p_{3/2}$, Zn $2p_{1/2}$, Cd $3d_{5/2}$, Cd $3d_{3/2}$, and S 2p for the alloyed $Zn_xCd_{1-x}S$ films are located at around 1022.5 eV, 1045.5 eV, 405.2 eV, 412.0 eV, and 162.7 eV, respectively, which are all in agreement with the corresponding binding energies of $Zn_xCd_{1-x}S$;[25,35,36] it provides a solid evidence that the as-deposited product is $Zn_xCd_{1-x}S$. The radii of the Zn^{2+} ions (0.74 Å) are smaller than those of the Cd^{2+} ions (0.97 Å), leading to shorter bond lengths of Zn–S than those of Cd–S. The local environment around Cd^{2+} ions would be changed due to the substitution of Zn^{2+} ions in place of Cd^{2+} ions in the CdS lattice. Therefore, the variation of the coordination environments around the S^{2-} ions would affect the position of the binding energy of S 2p, leading to a shift of the binding energy to high values as the number of Zn^{2+} ions increases. The area under the peaks was calibrated to obtain the Zn/Cd ratio, namely composition (x) values. The compositions of the ternary $Zn_xCd_{1-x}S$ films obtained by e-beam evaporation with the targets having various ZnS/CdS molar ratios of 2 : 8, 5 : 5, 7 : 3, 8 : 2, and 9 : 1 were calculated to be $x = 0.23$, 0.59, 0.72, 0.82, and 0.95, respectively, as shown in Table 1.

3.2. Crystallinity and microstructure

The crystallinity and microstructure of $Zn_xCd_{1-x}S$ films were characterized by TEM. The TEM images in Fig. 2a, c, and e show the film morphology after the deposited $Zn_xCd_{1-x}S$ films on 300 nm SiO_2/Si substrate were dispersed in ethanol. The selected-area electron-diffraction (SAED) patterns (insets in Fig. 2a, c, and e) confirm that the as-deposited films are polycrystalline. Combining the high-resolution TEM (HRTEM) images with the corresponding Fourier transform images in Fig. 2b, d, and f, the as-deposited $Zn_xCd_{1-x}S$ films with $x = 0.23$ and 0.59 are characterized to have the hexagonal wurtzite structure, whereas $Zn_xCd_{1-x}S$ films with $x = 0.82$ have the zinc blende structure. This phenomenon that the structure of the alloys is related to the composition was also reported by an other group.[21] Furthermore, the interplanar distances of $\{100\}$ for hexagonal $Zn_xCd_{1-x}S$ with $x = 0.23$ and 0.59 are 3.56 Å and 3.35 Å, respectively, confirming that the interplanar distances of $Zn_xCd_{1-x}S$ films vary with the composition x.

3.3. Crystal structure

The X-ray diffraction (XRD) measurements were further conducted to investigate the structure of all $Zn_xCd_{1-x}S$ samples with different x values, as shown in Fig. 3. Curves (a) and (g) are for the pure ZnS and CdS films, respectively, which correspond to the respective bulk zinc blende ZnS (JCPDS 77-2100) and wurtzite CdS (JCPDS 70-2553) crystals. Curves (b)–(f) are for the samples obtained by e-beam evaporation with the targets having various ZnS to CdS molar ratios of 9 : 1, 8 : 2, 7 : 3, 5 : 5, and 2 : 8, respectively. The XRD patterns revealed that the

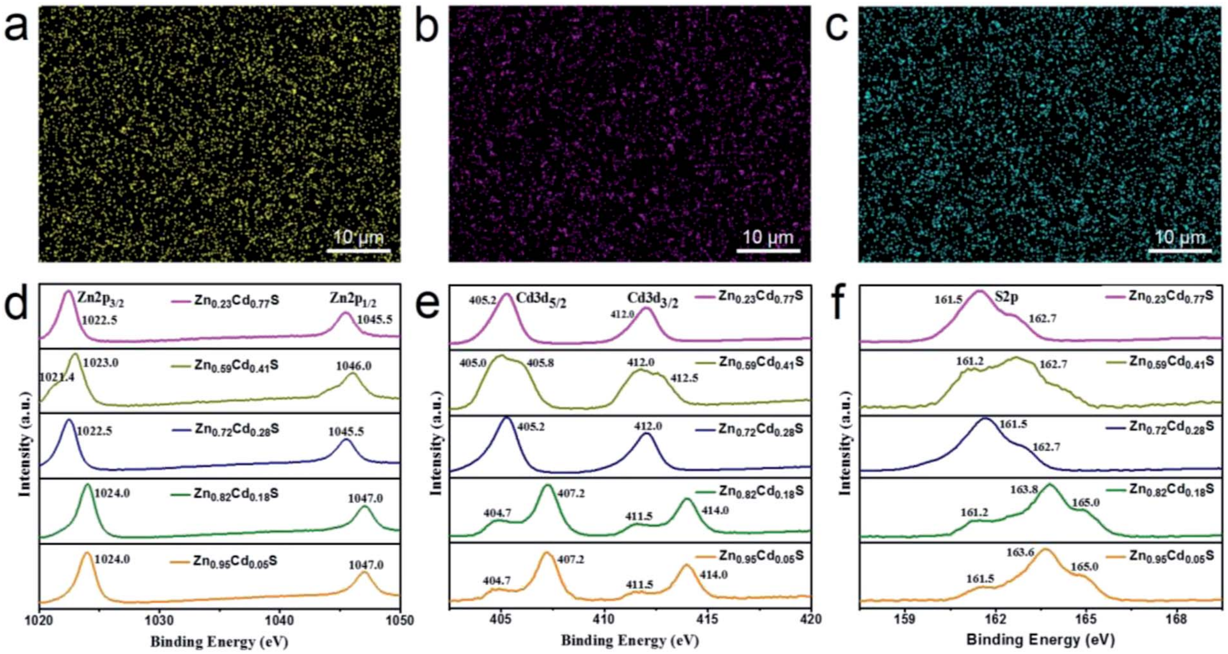

Fig. 1 EDX mapping of (a) Zn, (b) Cd, and (c) S conducted on the as-deposited $Zn_xCd_{1-x}S$ films on 300 nm SiO_2/Si substrate. XPS spectra of the as-deposited $Zn_xCd_{1-x}S$ films with different compositions: (d) Zn $2p_{3/2}$ and Zn $2p_{1/2}$, (e) Cd $3d_{5/2}$ and Cd $3d_{3/2}$, and (f) S 2p. It provides solid evidence that the as-deposited product is a $Zn_xCd_{1-x}S$ film.

ternary $Zn_xCd_{1-x}S$ films over the compositions of $x = 0.95$, 0.82, and 0.72 have the zinc blende structure, whereas the ternary films with the composition of $x = 0.59$ and 0.23 have the wurtzite structure. It can be observed that the XRD peaks of zinc blende structured and wurtzite structured $Zn_xCd_{1-x}S$ ternary films continuously shift to smaller angles from curves (a) to (d) and from curves (e) to (g), respectively, indicating that the lattice parameters of the films increase with of the decreasing composition x. The continuous peak shift further indicates that alloyed $Zn_xCd_{1-x}S$ films with modulated compositions between ZnS and CdS were successfully achieved by an e-beam evaporation method *via* changing the molar ratio of ZnS to CdS in the target, which may also rule out the phase separation of ZnS or CdS.[37,38]

Table 1 The XPS characteristic peaks of Zn 2p and Cd 3d are used for the composition estimation. The compositions of ternary $Zn_xCd_{1-x}S$ films obtained by e-beam evaporation with the targets having various ZnS/CdS molar ratios of 2 : 8, 5 : 5, 7 : 3, 8 : 2, and 9 : 1 are calculated to be $x = 0.23$, 0.59, 0.72, 0.82, and 0.95, respectively, by calibrating the area under the XPS peaks of Zn 2p and Cd 3d

Molar ratio of ZnS/CdS	Atomic percentage%			Film composition
	Zn 2p	Cd 3d	S 2p	
2/8	11.35	39.51	49.15	$Zn_{0.23}Cd_{0.77}S$
5/5	13.87	9.58	21.25	$Zn_{0.59}Cd_{0.41}S$
7/3	37.77	14.8	47.42	$Zn_{0.72}Cd_{0.28}S$
8/2	27.54	6.09	28.99	$Zn_{0.82}Cd_{0.18}S$
9/1	30.62	1.70	28.30	$Zn_{0.95}Cd_{0.05}S$

3.4. Energy gap

The UV-visible optical absorption spectra were acquired at room temperature to obtain the variation of light absorption for $Zn_xCd_{1-x}S$ films with different values of x, as shown in Fig. 4a. The spectra clearly show that the absorption edge is gradually shifted towards a longer wavelength with the decreasing value of x. As is known, the optical absorption is related to the electron excitation from the valance band to the conduction band. Therefore, the shift towards a longer wavelength indicates a decrease in the energy gap (E_g). Moreover, E_g can be attained by extrapolating the straight line plot of $(\alpha h\nu)^2$ *versus* $(h\nu)$ to the energy axis. The absorption coefficient (α) and the incident photon energy $h\nu$ are related by the following equation:[39,40]

$$\alpha h\nu = A(h\nu - E_g)^n \tag{1}$$

where A is a constant, E_g is the band gap of the material, and the exponent $n = 1/2$ for the material with direct band gap. The variation of $(\alpha h\nu)^2$ as a function of $h\nu$ is shown in Fig. 4b. Obviously, the obtained E_g of $Zn_xCd_{1-x}S$ films with different values of x continuously decreases with the decreasing value of x.

E_g of the alloyed $Zn_xCd_{1-x}S$ films are plotted in Fig. 4c as a function of the composition x. It can be seen that the variation of E_g with composition x slightly deviates from linear dependence, displaying a downward bowing. This character has also been reported for many alloyed films,[41–43] alloyed nanocrystals,[44] and alloyed 1D nanostructures.[19,21] In the case of the $Zn_xCd_{1-x}S$ system, the nonlinear variation of E_g can be represented as a quadratic function of the composition x:[19,45,46]

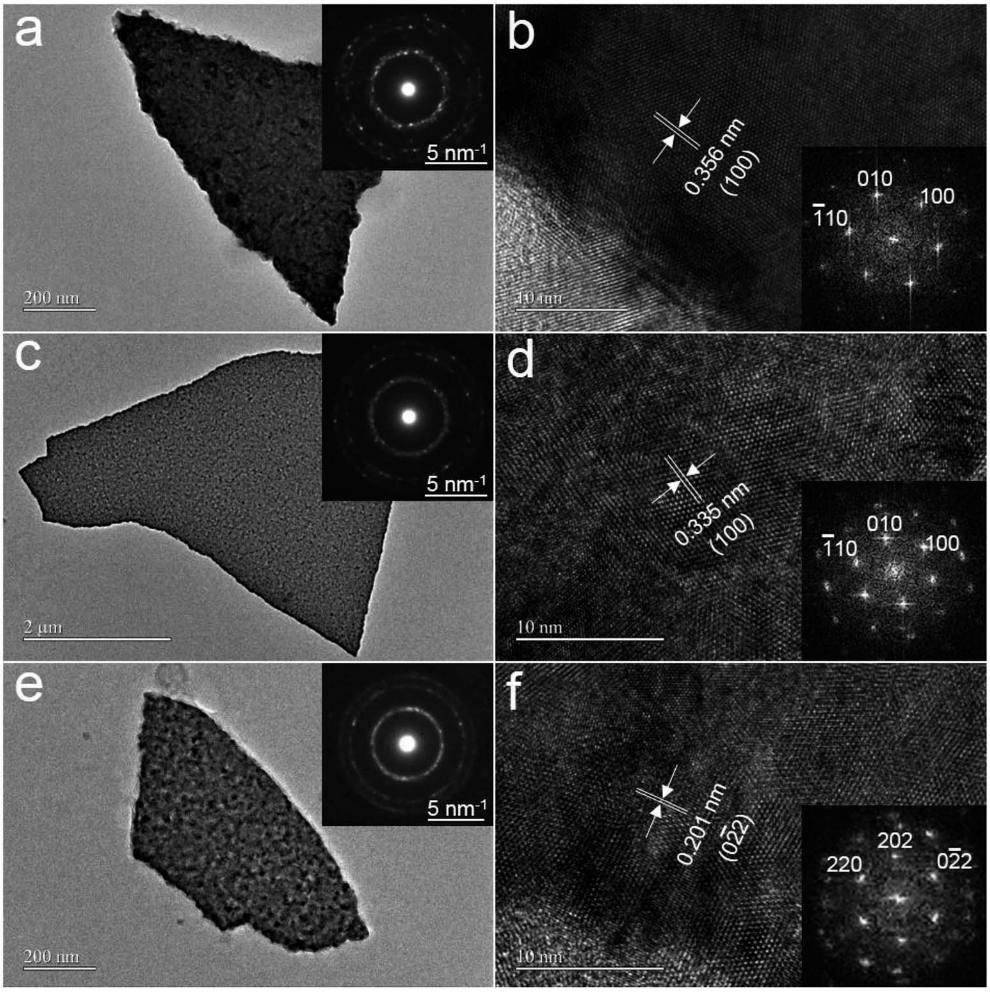

Fig. 2 TEM images of the as-deposited $Zn_xCd_{1-x}S$ films with (a) $x = 0.23$, (c) $x = 0.59$, and (e) $x = 0.82$. The inset is the corresponding SAED. HRTEM images of the $Zn_xCd_{1-x}S$ films with (b) $x = 0.23$, (d) $x = 0.59$, and (f) $x = 0.82$. The corresponding Fourier transform images (inset) show that $Zn_{0.23}Cd_{0.77}S$ and $Zn_{0.59}Cd_{0.41}S$ have a hexagonal wurtzite structure, whereas $Zn_{0.82}Cd_{0.18}S$ has a zinc blende structure. The interplanar distances of {100} for hexagonal $Zn_{0.23}Cd_{0.77}S$ and $Zn_{0.59}Cd_{0.41}S$ are 3.56 Å and 3.35 Å, respectively, confirming that the interplanar distances of $Zn_xCd_{1-x}S$ films vary with the composition x.

$$E_g(x) = xE_g(\mathrm{ZnS}) + (1 - x)E_g(\mathrm{CdS}) - x(1 - x)b \qquad (2)$$

where $E_g(x)$ is the energy gap of $Zn_xCd_{1-x}S$, $E_g(\mathrm{ZnS})$ is the energy gap of ZnS, $E_g(\mathrm{CdS})$ is the energy gap of CdS, and b is the bowing parameter. The second-order polynomial fitting of the experimental results, as shown in Fig. 4c (solid line), gives the following quadratic expression:

$$E_g(x) = 2.43 + 0.68x + 0.50x^2 \qquad (3)$$

which yields the bowing parameter of $b = 0.50$ eV. The obtained bowing parameter is similar to the value reported in the previous studies on $Zn_xCd_{1-x}S$.[19,42,43] Note that the slight variation of energy gaps resulted from different crystal structure (zinc blende or wurtzite) of alloyed $Zn_xCd_{1-x}S$ films is ignored.

3.5. Photoconductive properties

After graphene films are transferred on the alloyed $Zn_xCd_{1-x}S$ films on the 300 nm SiO_2/Si substrate, band-tunable photodetectors based on graphene/alloyed $Zn_xCd_{1-x}S$ film hybrids can be achieved. To fabricate graphene/alloyed $Zn_xCd_{1-x}S$ film-based field effect transistors, Cr/Au (10 nm/100 nm) electrodes with a length of 20 μm and width of 500 μm were deposited by e-beam evaporation through a shadow mask. After light was focused on the channel, the photoconductive properties of graphene/$Zn_xCd_{1-x}S$ film hybrids could be investigated, schematically shown in the inset of Fig. 5a. Typical transfer characteristics of the back-gated transistors for graphene transferred on the $Zn_xCd_{1-x}S$ films show a hole-dominated transport without the appearance of a Dirac point. This probably arises from the p-doping of oxygen in air.[9,14,32] Upon 365 nm light irradiation, the source-drain current (I_{sd}) obviously increases regardless of the gate bias (V_g) for all $Zn_xCd_{1-x}S$ films with different compositions (Fig. 5). The increase in the hole-dominated current in the graphene channel means that the holes transfer from the $Zn_xCd_{1-x}S$ film to graphene.[9,14,15] Therefore, the working mechanism for a graphene/$Zn_xCd_{1-x}S$ film hybrid photodetector is the same as that for

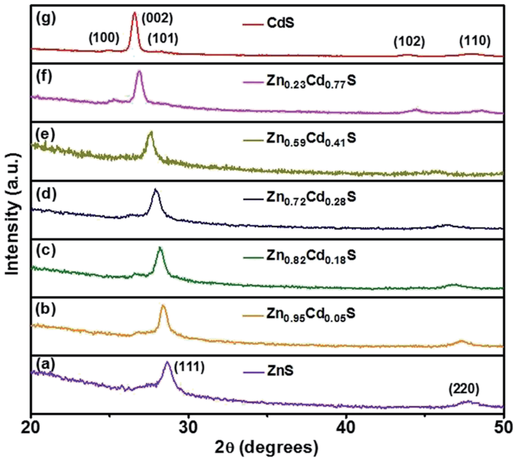

Fig. 3 XRD pattern of the $Zn_xCd_{1-x}S$ films with different values of x. The XRD patterns show that the ternary $Zn_xCd_{1-x}S$ films over compositions of $x = 1$, 0.95, 0.82, and 0.72 have a zinc blende structure, whereas the ternary films with composition of $x = 0.59$, 0.23, and 0 have a wurtzite structure. The continuous peak shifting indicates that alloyed $Zn_xCd_{1-x}S$ films with modulated compositions between ZnS and CdS were successfully achieved.

a graphene/ZnS film hybrid photodetector, which was illustrated in a previous study.[17] Fig. 6 depicts a time-dependent response of graphene/alloyed $Zn_xCd_{1-x}S$ film hybrid-based device by switching light illumination with different wavelength yet at the same power of 1 mW cm^{-2} on and off periodically at a fixed voltage of 1.0 V. The current increases to a stable value of certain mA upon illumination, and then decreases to the initial value when the light is turned off, which shows good stability for the devices based on graphene/alloyed $Zn_xCd_{1-x}S$ film hybrids. The responsivity and response time of the graphene/II–VI semiconductor film-based photodetectors can be observed in a previous study,[17] and we only focus on the band tunability of the devices based on graphene/alloyed $Zn_xCd_{1-x}S$ film hybrids in this study. All the photodetectors show that the photocurrents depend on the incident wavelength, with the largest values for the detectors with all values of x being located at around 365 nm (Fig. 6). In addition, the values of the largest photocurrent for the ternary $Zn_xCd_{1-x}S$ $(0 < x < 1)$ films are all higher than those of the binary compound CdS $(x = 0)$ and ZnS $(x = 1)$ films. Ren *et al.* also reported a similar phenomenon that the largest photocurrents of the ternary $InAs_xP_{1-x}$ $(0 < x < 1)$ nanowires are larger than those of the InP $(x = 0)$ and InAs $(x = 1)$ nanowires.[28]

To attain the detailed wavelength related spectral response for the photodetector based on graphene/alloyed $Zn_xCd_{1-x}S$ films, wavelength-dependent photocurrents of the devices were measured with the incident light wavelength scanned from 365 to 585 nm under a bias voltage of 1 V and a light intensity of 1 mW cm^{-2}, as shown in Fig. 7. Note that the photocurrents calculated from the detectors based on graphene/alloyed $Zn_xCd_{1-x}S$ films with different compositions are normalized. Two types of variation tendency of the spectral response for graphene/alloyed $Zn_xCd_{1-x}S$ film hybrids are clearly observed.

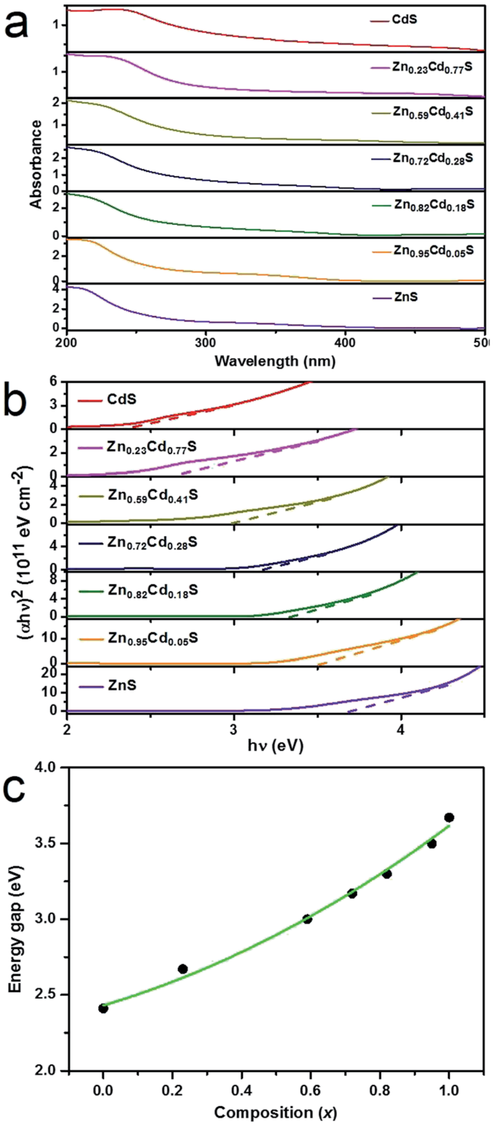

Fig. 4 (a) UV-visible optical absorption spectra of the $Zn_xCd_{1-x}S$ films with different composition x on a quartz substrate. (b) The variation of $(\alpha h\nu)^2$ as function of $h\nu$ for the $Zn_xCd_{1-x}S$ films with different composition x. E_g can be attained by extrapolating the straight line plot of $(\alpha h\nu)^2$ *versus* $(h\nu)$ to the energy axis. (c) E_g of the alloyed $Zn_xCd_{1-x}S$ films as a function of the composition x. It can be seen that the variation of E_g with composition x slightly deviates from linear dependence, displaying downward bowing.

For graphene/$Zn_xCd_{1-x}S$ film with compositions $x = 1$, 0.95, 0.82, and 0.72, the photocurrent increased with the decreasing excited wavelength, which is in good agreement with the results of the ZnS-based photodetector.[5] However, for graphene/$Zn_xCd_{1-x}S$ film with compositions $x = 0.59$, 0.23, and 0, the photocurrent increased with the decreasing excited wavelength as the wavelength is shorter than the value corresponding to the energy gap, and then decreased with the decreasing wavelength, and finally increased with the decreasing wavelength, namely presenting a peak and a valley. The different variation tendency of the spectral response was attributed to the different absorption behavior of the $Zn_xCd_{1-x}S$ film with different

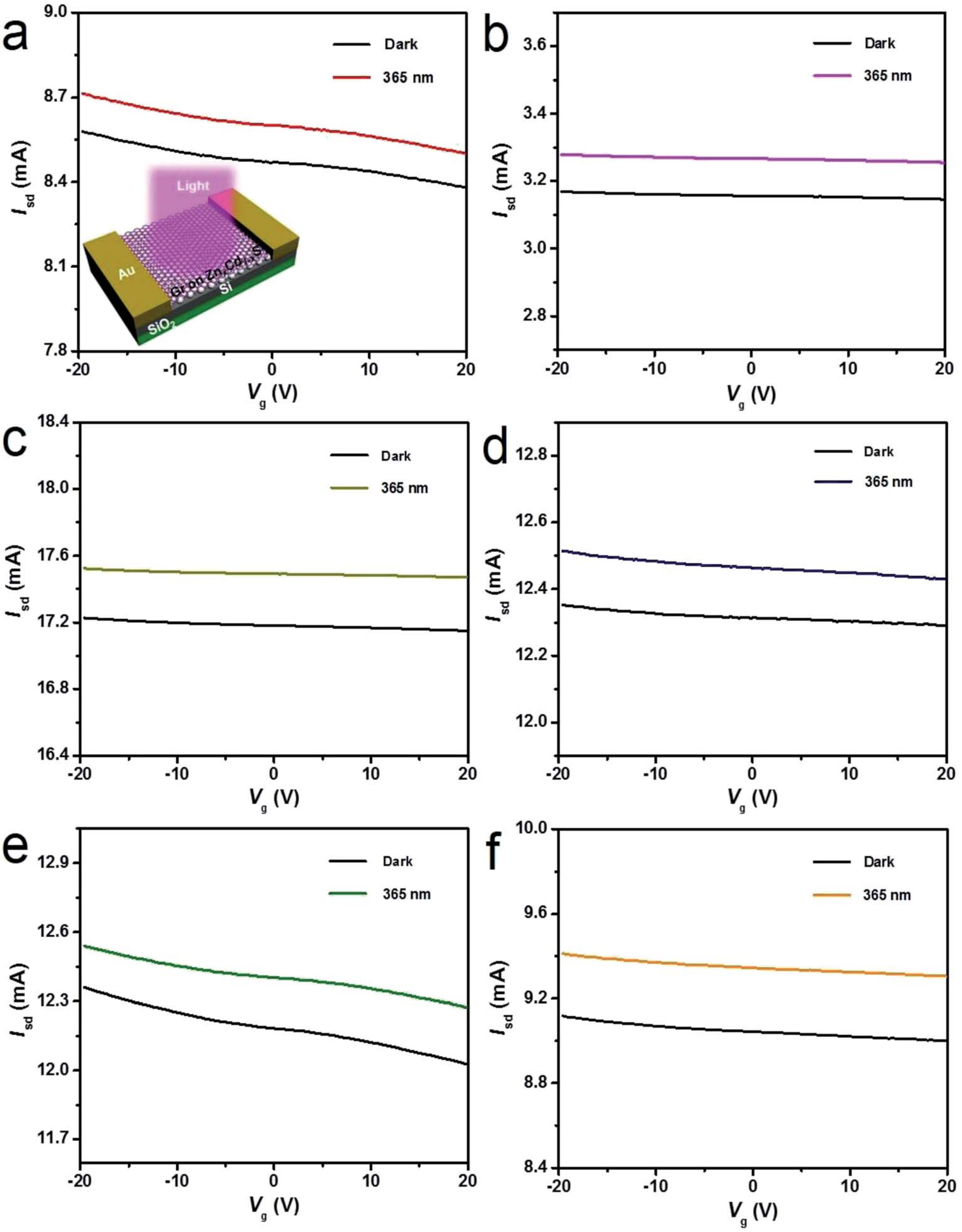

Fig. 5 Typical transfer characteristics of the back-gated transistors for graphene transferred on $Zn_xCd_{1-x}S$ films with compositions (a) $x = 0$, (b) $x = 0.23$, (c) $x = 0.59$, (d) $x = 0.72$, (e) $x = 0.82$, and (f) $x = 0.95$, showing a hole-dominated transport. The inset shows the scheme of graphene/$Zn_xCd_{1-x}S$ film hybrid-based photodetector. Upon 365 nm light irradiation, I_{sd} obviously increases regardless of V_g for all $Zn_xCd_{1-x}S$ films with different compositions.

compositions. For $Zn_xCd_{1-x}S$ film with composition $x = 0.59$, 0.23, and 0, there is an obvious peak locating at *hν* around the corresponding energy gap of $Zn_xCd_{1-x}S$, whereas for $Zn_xCd_{1-x}S$ film with a composition $x = 1$, 0.95, 0.82, and 0.72, the peak does not appear obvious (Fig. 4b). Choi *et al.* reported that the variation tendency of spectral response for $CdSe_xS_{1-x}$ nanowire-based photodetectors only includes a peak.[27] This is because the absorption curve of $CdSe_xS_{1-x}$ nanowires only shows an absorption peak without an absorption edge, which exists in the absorption curve for the as-deposited $Zn_xCd_{1-x}S$ film with all values of *x*. Regardless of the variation tendency of the spectral response for the photodetector, the important point is that the cut-off wavelength is gradually blue shifted from 585 to 410 nm as the *x* value increases from 0 (CdS) to 1 (ZnS). It is well known that the cut-off wavelength of the spectral response relates to the absorption wavelength at the band edge (band-to-band transition).[47,48] The observed variation of the cut-off wavelength with the composition *x* in the alloyed $Zn_xCd_{1-x}S$ films demonstrates the successful modulation of the optoelectronic response range of the devices by means of bandgap engineering of the $Zn_xCd_{1-x}S$ films.

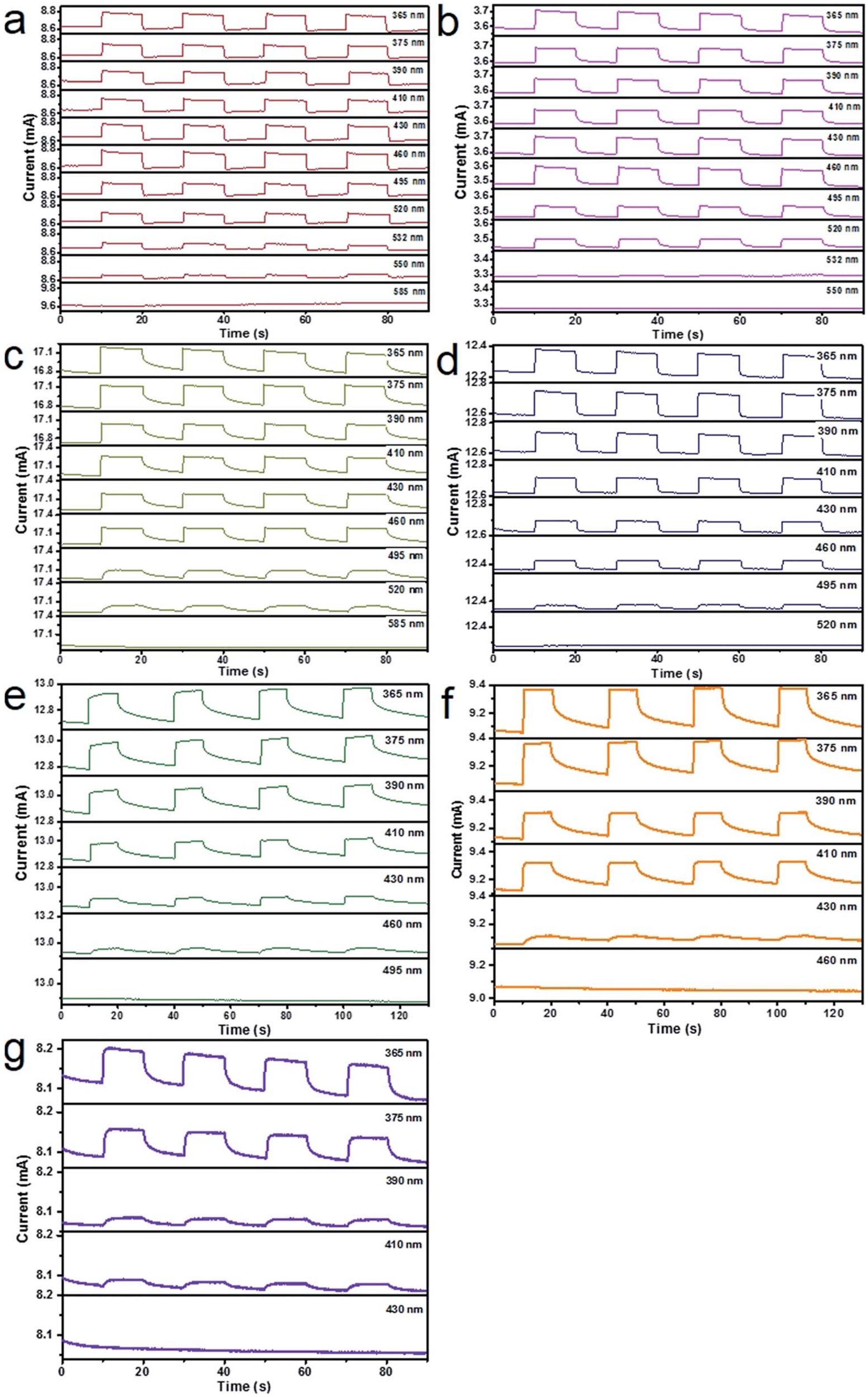

Fig. 6 Time-dependent response of graphene/alloyed $Zn_xCd_{1-x}S$ film hybrid-based photodetectors with compositions (a) $x = 0$, (b) $x = 0.23$, (c) $x = 0.59$, (d) $x = 0.72$, (e) $x = 0.82$, (f) $x = 0.95$, and (g) $x = 1$, by switching light illumination with different wavelengths but the same power of 1 mW cm^{-2} on and off periodically at a fixed voltage of 1.0 V. All the photodetectors show that the photocurrents depend on the incident wavelength, with the largest values for the detectors with all values of x being located at around 365 nm.

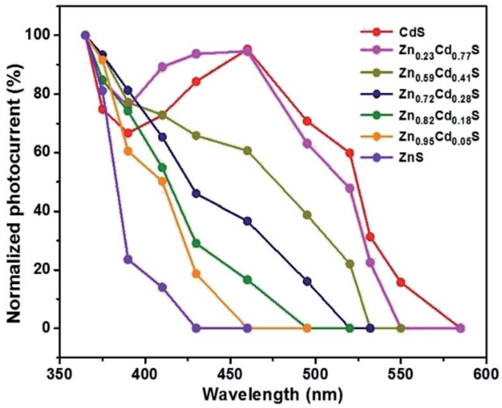

Fig. 7 Wavelength related spectral response for the graphene/$Zn_xCd_{1-x}S$ film-based photodetectors measured with the incident light wavelength scanned from 365 to 585 nm under a light intensity of 1 mW cm^{-2}. The cut-off wavelength is gradually blue shifted from 585 to 410 nm as the x value increases from 0 (CdS) to 1 (ZnS). The observed variation of the cut-off wavelength with the composition x demonstrates the successful modulation of the optoelectronic response range of the devices *via* the bandgap engineering of $Zn_xCd_{1-x}S$.

4. Conclusions

In summary, alloyed $Zn_xCd_{1-x}S$ ($0 \leq x \leq 1$) films with complete compositional tunability were successfully prepared by e-beam evaporation by changing the molar ratio of ZnS to CdS in the target. The UV-visible optical absorption measurements show that the composition-dependent band-edge absorption is generated in the as-prepared alloyed $Zn_xCd_{1-x}S$ films with the energy gaps continuously shifted from 2.41 eV ($x = 0$, CdS) to 3.67 eV ($x = 1$, ZnS). After graphene is transferred on the alloyed $Zn_xCd_{1-x}S$ films, band-tunable photodetectors are achieved based on the graphene/alloyed $Zn_xCd_{1-x}S$ film hybrids with the cut-off wavelength gradually changing from 410 nm to 580 nm. Obviously, the method introduced in this study can be extended to the fabrication of other graphene/alloyed ternary film hybrid-based photodetectors with band tunability in the visible and infrared region.

Acknowledgements

This research was financially supported by the National Natural Science Foundation of China (No. 21473047 and 51471162) and the Fundamental Research Funds for the Central Universities (2015HGCH0007).

Notes and references

1 M. Razeghi and A. J. Rogalski, *Appl. Phys.*, 1996, **79**, 7433–7473.
2 M. S. Shur and A. Zukauskas, *NATO Sci. Ser., II*, 2004, **144**, 1.
3 S. A. McDonald, G. Konstantatos, S. G. Zhang, P. W. Cyr, E. J. D. Klem, L. Levina and E. H. Sargent, *Nat. Mater.*, 2005, **4**, 138.
4 J. S. Jie, W. J. Zhang and Y. Jiang, *Appl. Phys. Lett.*, 2006, **89**, 133118.
5 X. S. Fang, Y. Bando, M. Y. Liao, U. K. Gautam, C. Y. Zhi, B. Dierre, B. D. Liu, T. Y. Zhai, T. Sekiguchi, Y. Koide and D. Golberg, *Adv. Mater.*, 2009, **21**, 2034–2039.
6 L. Li, P. C. Wu, X. S. Fang, T. Y. Zhai, L. Dai, M. Y. Liao, Y. Koide, H. Q. Wang, Y. Bando and D. Golberg, *Adv. Mater.*, 2010, **22**, 3161.
7 X. M. Geng, L. Niu, Z. Y. Xing, R. S. Song, G. T. Liu, M. T. Sun, G. S. Cheng, H. J. Zhong, Z. H. Liu, Z. J. Zhang, L. F. Sun, H. X. Xu, L. Lu and L. W. Liu, *Adv. Mater.*, 2010, **22**, 638.
8 Y. Lin, K. Zhang, W. F. Chen, Y. D. Liu, Z. G. Geng, J. Zeng, N. Pan, L. F. Yan, X. P. Wang and J. G. Hou, *ACS Nano*, 2010, **6**, 3033–3038.
9 G. Konstantatos, M. Badioli, L. Gaudreau, J. Osmond, M. Bernechea, F. P. G. de Arquer, F. Gatti and F. H. L. Koppens, *Nat. Nanotechnol.*, 2012, **7**, 363–368.
10 W. H. Guo, S. G. Xu, Z. F. Wu, N. Wang, M. M. T. Loy and S. W. Du, *Small*, 2013, **18**, 3031–3036.
11 Y. T. Kim, H. W. Shin, Y. S. Ko, T. K. Ahn and Y. U. Kwon, *Nanoscale*, 2013, **5**, 1483–1488.
12 K. H. Zheng, F. B. Meng, L. Jiang, Q. Y. Yan, H. H. Hng and X. D. Chen, *Small*, 2013, **12**, 2076–2080.
13 J. H. Li, Y. Niu, Z. J. Zheng and F. Yan, *Adv. Mater.*, 2014, **26**, 5239–5273.
14 D. Y. Zhang, L. Gan, Y. Cao, Q. Wang, L. M. Qi and X. F. Guo, *Adv. Mater.*, 2012, **24**, 2715–2720.
15 Z. H. Sun, Z. K. Liu, J. H. Li, G. A. Tai, S. P. Lau and F. Yan, *Adv. Mater.*, 2012, **24**, 5878–5883.
16 X. Liu, N. Z. Liu, M. J. Liu, Z. Tao, W. J. Kuang, X. B. Ji, J. Chen, W. Lei, Q. Dai and C. Li, *Nanoscale*, 2015, **7**, 4242–4249.
17 F. Huang, F. X. Jia, C. Y. Cai, Z. H. Xu, C. J. Wu, Y. Ma, G. T. Fei and M. Wang, *Sci. Rep.*, 2016, **6**, 28943.
18 M. Wang, G. T. Fei, Y. G. Zhang, M. G. Kong and L. D. Zhang, *Adv. Mater.*, 2007, **19**, 4491–4494.
19 Y. K. Liu, J. A. Aapien, Y. Y. Shan, C. Y. Geng, C. S. Lee and S. T. Lee, *Adv. Mater.*, 2005, **17**, 1372–1377.
20 A. L. Pan, H. Yang, R. B. Liu, R. C. Yu, B. S. Zou and Z. L. Wang, *J. Am. Chem. Soc.*, 2005, **127**, 15692.
21 R. Venugopal, P. I. Lin and Y. T. Chen, *J. Phys. Chem. B*, 2006, **110**, 11691.
22 T. Kuykendall, P. Ulrich, S. Aloni and P. D. Yang, *Nat. Mater.*, 2007, **6**, 951–956.
23 M. N. Huang, J. H. Yu, C. S. Deng, Y. H. Huang, M. G. Fan, B. Li, Z. F. Tong, F. Y. Zhang and L. H. Dong, *Appl. Surf. Sci.*, 2016, **365**, 227–239.
24 J. Chen, B. B. Ding, T. Y. Wang, F. Li, Y. Zhang, Y. L. Zhao and H. S. Qian, *J. Mater. Sci.: Mater. Electron.*, 2014, **25**, 4103–4109.
25 X. Xu, R. J. Lu, X. F. Zhao, Y. Zhu, S. L. Xu and F. Z. Zhan, *Appl. Catal., B*, 2012, **125**, 11–20.
26 T. Takahashi, P. Nichols, K. Takei, A. C. Ford, A. Jamshidi, M. C. Wu, C. Z. Ning and A. Javey, *Nanotechnology*, 2012, **23**, 045201.
27 Y. J. Choi, K. S. Park and J. G. Park, *Nanotechnology*, 2010, **21**, 505605.

28 P. Y. Ren, W. Hu, Q. L. Zhang, X. L. Zhu, X. J. Zhuang, L. Ma, X. P. Fan, H. Zhou, L. Liao, X. F. Duan and A. L. Pan, *Adv. Mater.*, 2014, **26**, 7444–7449.

29 X. W. Wang, H. W. Tian, W. T. Zheng and Y. C. Liu, *Mater. Lett.*, 2013, **109**, 100–103.

30 X. W. Wang, H. W. Tian, X. Q. Cui, W. T. Zheng and Y. C. Liu, *Dalton Trans.*, 2014, **43**, 12894.

31 F. Xu, D. D. Bai, S. Y. Han, D. P. Wu, Z. Y. Gao and K. Jiang, *Sens. Actuators, B*, 2014, **203**, 89–94.

32 M. Wang, S. K. Jang, W. J. Jang, M. Kim, S. Y. Park, S. W. Kim, S. J. Kahng, J. Y. Choi, R. S. Ruoff, Y. J. Song and S. Lee, *Adv. Mater.*, 2013, **25**, 2746–2752.

33 M. Wang, L. Fu, L. Gan, C. H. Zhang, M. Rummeli, A. Bachmatiuk, K. Huang, Y. Fang and Z. F. Liu, *Sci. Rep.*, 2013, **3**, 1238.

34 C. Y. Cai, F. X. Jia, A. L. Lei, F. Huang, Z. H. Xu, L. Z. Qiu, Y. Q. Chen, G. T. Fei and M. Wang, *Carbon*, 2016, **98**, 457–462.

35 D. L. Han, J. Cao, S. Yang, J. H. Yang, B. J. Wang, L. Fan, Q. Y. Liu, T. T. Wang and H. F. Niu, *Dalton Trans.*, 2014, **43**, 11019–11026.

36 H. M. Wang, Z. Chen, Q. Cheng and L. X. Yuan, *J. Alloys Compd.*, 2009, **478**, 872–875.

37 X. H. Zhong, Y. Y. Feng, W. Knoll and M. Y. Han, *J. Am. Chem. Soc.*, 2003, **125**, 13559–13563.

38 X. H. Zhong, M. Y. Han, Z. L. Dong, T. J. White and W. Knoll, *J. Am. Chem. Soc.*, 2003, **125**, 8589–8594.

39 P. F. Luo, Z. F. Liu, W. Xia, C. C. Yuan, J. G. Cheng and Y. W. Lu, *ACS Appl. Mater. Interfaces*, 2015, **7**, 2708–2714.

40 M. Ashokkumar and S. Muthukumaran, *J. Lumin.*, 2015, **162**, 97–103.

41 C. T. Hsu, *J. Cryst. Growth*, 1998, **193**, 33–38.

42 D. Barreca, A. Gasparotto, C. Maragno, E. Tondello and C. Sada, *Chem. Vap. Deposition*, 2004, **10**, 229–236.

43 G. Perna, S. Pagliara, V. Capozzi, M. Ambrico and T. Ligonzo, *Thin Solid Films*, 1999, **349**, 220–224.

44 L. A. Swafford, L. A. Weigand, M. J. Bowers, J. R. McBride, J. L. Rapaport, T. L. Watt, S. K. Dixit, L. C. Feldman and S. J. Rosenthal, *J. Am. Chem. Soc.*, 2006, **128**, 12299–12306.

45 M. C. Baykul and N. Orhan, *Thin Solid Films*, 2010, **518**, 1925–1928.

46 W. Li, J. Y. Yang, Z. Sun, L. H. Feng, J. Q. Zhang and L. L. Wu, *Int. J. Photoenergy*, 2011, **2011**, 969214.

47 L. F. Hu, J. Yan, M. Y. Liao, H. J. Xiang, X. G. Gong, L. D. Zhang and X. S. Fang, *Adv. Mater.*, 2012, **24**, 2305–2309.

48 S. M. Sze and K. K. Ng, *Physics of Semiconductor Devices*, Wiley, Hoboken, NJ, 3rd edn, 2007.